Invited Paper

Beam filamentation and its control in high-power semiconductor lasers

John R. Marciante

Air Force Research Laboratory, Directed Energy Directorate
AFRL/DELS, 3550 Aberdeen Avenue SE, Kirtland AFB, NM 87117-5776

Govind P. Agrawal

Institute of Optics, University of Rochester
Rochester, NY 14627

ABSTRACT

We experimentally measure the first-order spatio-temporal characteristics of filamentation and discover effects of the stripe width. We use an analytic theory to explain and reproduce these results through an expression for the filament gain, in which contributions of various mechanisms can clearly be seen. Through this model and computer simulations, we determine the stability boundaries of the material parameters for which the device will not exhibit filamentary tendencies. We then propose a new method of controlling filamentation using below-bandgap semiconductor nonlinearities. With simulations, we determine under what conditions this imposed nonlinearity can counteract the carrier-induced self-focusing inside the active region.

Keywords: beam filamentation, broad-area lasers, dynamics, high-power lasers, laser stability, optical propagation in nonlinear media, semiconductor lasers, spatio-temporal instabilities

1. INTRODUCTION

High-power lasers are useful in a myriad of applications such as laser surgery, optical data recording, free-space and fiber-optic communications, remote sensing and environmental testing, wavelength conversion, industrial cutting and welding, and electro-optic countermeasures. Semiconductor lasers are ideal for many of these applications for many reasons, such as compactness, durability, high efficiency, integrability, and low cost due to mass producibility. For semiconductor lasers to achieve the power levels required for many of these applications, several issues which limit the performance of such high-power devices must be resolved. In this paper, we turn our attention to beam filamentation.

Due to saturation of the semiconductor medium, the spatial gain profile can become distorted by a dip in the local carrier density where the light is most intense. This dip in the carrier density, known as spatial hole burning, causes a local increase in the refractive index, which leads to self-focusing of the light[1]. For broad-area gain regions, the light has no lateral confinement, so self-focusing tendencies can break up the lateral mode profile into multiple filaments. As with array architectures, this filamented beam cannot be cleanly focused into a single spot, but rather spreads its power into multiple far-field lobes, thus limiting the useful output power of the device.

As applications drive towards higher output powers, the filamentation issue has resurfaced in the context of amplifiers, which have a lower tendency to filament due to lack of counterpropagating waves[2]. Recent studies have investigated the propagation[3-5] and initiation[6] of filamentation in semiconductor amplifiers, but the analyses are primarily demonstrative with limited application to lasers. Another group investigated spatio-temporal chaos in semiconductor lasers[7, 8], but the focus was on a demonstration of chaotic behavior, unstable resonator analysis, and many-body effects.

Part of the SPIE Conference on Physics and Simulation of Optoelectronic Devices VI
San Jose, California • January 1998 SPIE Vol. 3283 • 0277-786X/98/$10.00

2. MEASURING BEAM FILAMENTATION

The samples used for the measurements[9] were two sets of quantum-well lasers with 50 μm stripe widths, one set operating at 808 nm and the other at 980 nm. The linewidth-enhancement factors for these devices are known to be near $\alpha \approx 4$ (±1) for AlGaAs lasers operating near 808 nm[10-13] and $\alpha \approx 2$ (± 0.5) for InGaAs lasers operating near 980 nm[13-16]. Light emitted from the devices was imaged onto a photodiode array to display the near-field profile, from which the spatial information could be extracted. As the injection current was varied, the devices displayed either a multiple-lobed filamentary pattern, noted by deep modulation and the clarity of independent spatial lobes, or exhibited a varying spatial pattern consisting of several spatial frequencies, resulting in a reduced modulation depth on our slow photodiode array. To ensure that the spatial data was extracted correctly, the injection current was chosen such that the modulation depth of a given filamentation pattern was maximum. In this way, the pump level for which a given spatial pattern dominates could be accurately determined.

In Fig. 1, we plot the dominant filament spacing for the two sets of devices as a function of the pump level r defined as $r = J/J_{th}$, where J is the injected current density and J_{th} is its value at threshold. The solid lines in Fig. 1 are fit to the experimental data from a theoretical model as discussed in Section 3. Several trends are evident in Fig. 1. First, the filament spacing decreases with increasing pumping level, or more practically, more filaments fit under the current stripe contact as the current is increased. Since diffractive spreading becomes increasingly stronger as the filament width becomes smaller, this observation is a clear indication that increasing the pumping level increases the severity of filamentation. The second trend shown in Fig. 1 is that the filament spacing is smaller for larger values of the linewidth-enhancement factor α. This observation is indirect evidence that self-focusing induced by spatial-hole burning is responsible for filamentation. While it is well known that both pumping level and the linewidth-enhancement factor contribute to the increased severity of filamentation, Fig. 1 shows that this increase is directly correlated with an increase in the filament spacing.

To confirm the spatio-temporal nature of filamentation, one must make temporal or spectral measurements together with the spatial measurements shown in Fig. 1. By splitting off a portion of the light before it was sent to the photodiode array, we measured the spectral properties of the filamented beam. In this branch, the light was sent through astigmatic collimation optics, an isolator, and then finally imaged onto a fast photodiode, whose signal was sent to a microwave spectrum analyzer. Any temporal fluctuations in the optical field inevitably lead to relaxation oscillations, resulting in a well-known peak at the relaxation-oscillation frequency Ω_{rel}. However, our measurements show that another frequency was dominant in the intensity noise spectrum of the laser. We refer to this frequency at the filamentation frequency Ω_{fil}. Figure 2 shows the evolution of the relaxation-oscillation and filamentation frequencies as a function of the pump level for a 980 nm laser. The upper curve was fit to a function of the form $A\sqrt{r-1}$, where A is a fitting parameter, while the lower curve was linearly fit to the experimental data by using the theoretical model discussed in

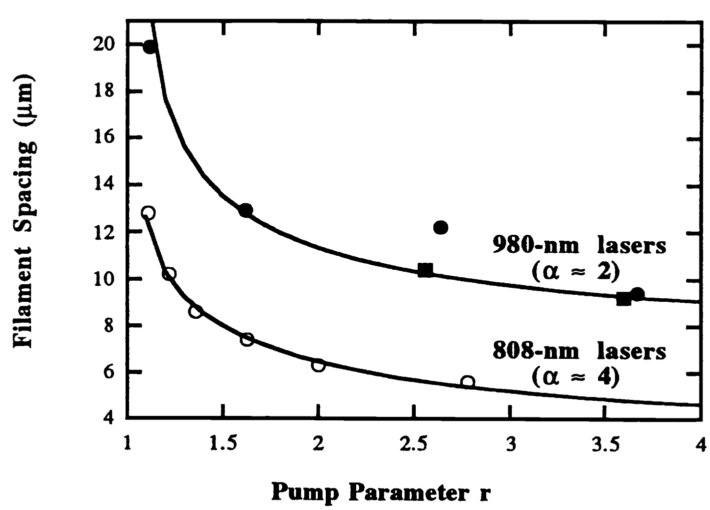

FIGURE 1. Measured filament spacing as a function of pump level $r = J/J_{th}$ for 980-nm (solid circles and squares) and 808-nm (empty circles) semiconductor lasers with a 50-μm stripe width. Solid lines are fitted using the theoretical model discussed in Section 3.

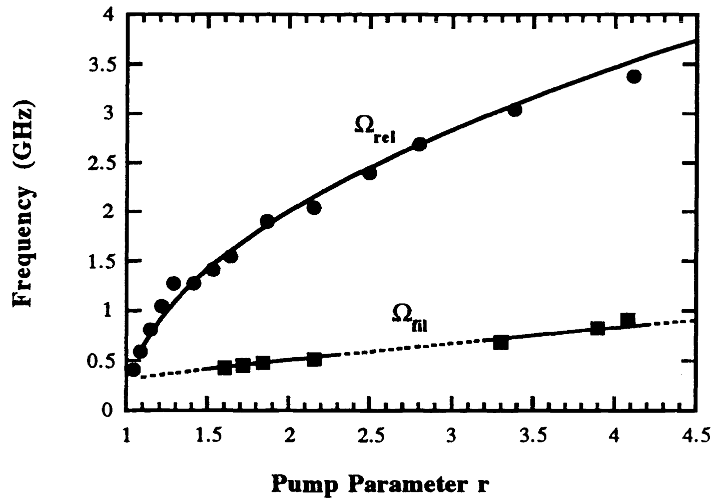

FIGURE 2. Measured variation of the relaxation-oscillation and filament frequencies, Ω_{rel} and Ω_{fil} respectively, with then pump level $r = J/J_{th}$ for a 980-nm laser. The curves are fitted using the theoretical models discussed in the text.

Section 3. The data indicate that spatial filamentation is accompanied by self-pulsing at a frequency in the 0.5-1.0 GHz range. This periodic modulation of the steady state is a result of the interplay between the nonlinear and diffractive effects that occur during propagation within the semiconductor laser medium.

As discussed earlier, the near field of the laser does not always show well-separated and nearly identical filaments. In these regions, the spectral data does not show a clear indication of Ω_{fil} (shown dashed in Fig. 2). The dashed region for $1 < r < 1.5$ is easily understood by noting that the laser is close enough to threshold and its output power is low enough that α-induced self-focusing has yet to produce filamentation. Near $r = 1.6$, the nonlinear effects become strong enough that the laser enters a self-pulsing regime in which the optical intensity is also spatially modulated. As the pump current was increased beyond this range, the filament frequency

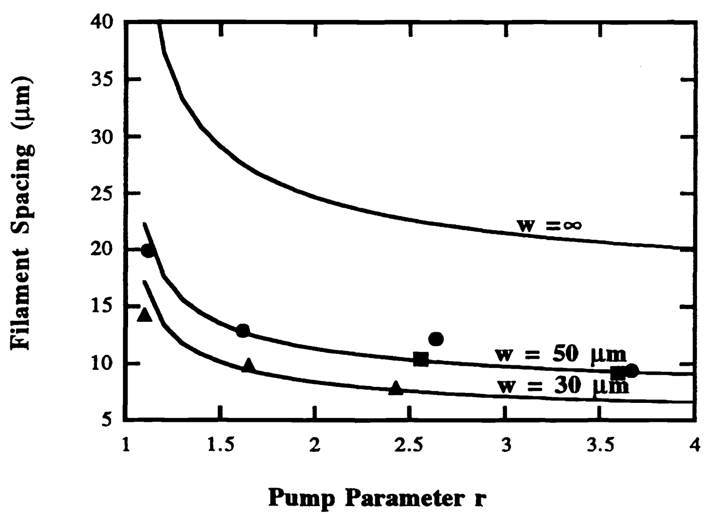

FIGURE 3. Measured filament spacing as a function of pump level r for 50-μm and 30-μm stripe-width lasers (α ≈ 2), and the theoretical prediction for infinite stripe-width lasers (α = 2).

re-emerged accompanied by another dominant spatial pattern (i.e. one more filament than was present in the fundamental pattern). For this pumping range, the peak at the filament frequency was rather broad. The broad-band nature of the intensity-noise spectrum suggests an underlying transition towards chaos. Further increase in pump indeed leads confirms this transition for $r > 4$. This noise spectrum shows not only two broad peaks located at Ω_{rel} and Ω_{fil} but also another broad peak located at $\Omega_{rel} - 2\Omega_{fil}$, in support of our hypothesis of a quasi-periodic route to chaos. Further increase in pump leads to a broadband, nearly featureless spectrum, as expected in the chaotic domain. Since the laser is chaotic both spatially and temporally, we refer to this behavior as spatio-temporal chaos.

The linear scaling needed for a quantitative fit to the model is attributed to the finite stripe width of our lasers. To test this hypothesis further, we performed the same spatial measurements of the dominant filament spacing on a 980-nm laser from the same epitaxial wafer as the other 980 nm lasers ($\alpha \approx 2$), but with a narrower stripe width of 30 μm. The results are displayed in Fig. 3, along with previous measurements of the 50-μm-stripe lasers at 980 nm and theoretical predictions for $\alpha = 2$. From this figure, we see that the effect of a finite stripe width is to squeeze the filaments more tightly together; the narrower the stripe, the more closely spaced the filaments become. Figure 3 suggests that measurements on a laser with a wide enough current stripe (> 200 μm) should agree quite well with the theoretical predictions both qualitatively and quantitatively.

3. MODELLING BEAM FILAMENTATION

In this paper, we will use two methods to model the semiconductor laser, one being an analytic approach, the other numerical. We characterize the semiconductor laser with the following coupled, nonlinear equations

$$\frac{\partial E_f}{\partial z} + \frac{1}{v_g}\frac{\partial E_f}{\partial t} = \frac{i}{2k}\frac{\partial^2 E_f}{\partial x^2} + \left[\frac{1}{2}\Gamma(1-i\alpha)g(N) - \frac{\alpha_{int}}{2} + in_2k_0(|E_f|^2 + 2|E_b|^2)\right]E_f, \tag{1}$$

$$-\frac{\partial E_b}{\partial z} + \frac{1}{v_g}\frac{\partial E_b}{\partial t} = \frac{i}{2k}\frac{\partial^2 E_b}{\partial x^2} + \left[\frac{1}{2}\Gamma(1-i\alpha)g(N) - \frac{\alpha_{int}}{2} + in_2k_0(|E_b|^2 + 2|E_f|^2)\right]E_b, \tag{2}$$

$$\frac{\partial N(x,z,t)}{\partial t} - D\frac{\partial^2 N}{\partial x^2} = \frac{J(x,z)}{qd} - \frac{N}{\tau_{nr}} - BN^2 - \frac{\Gamma g(N)}{\hbar\omega}\left(|E_f|^2 + |E_b|^2\right). \tag{3}$$

where E_f and E_b represent the forward and backward traveling waves of frequency ω respectively, N represents the carrier density, and the field and carriers are coupled through the gain $g(N) = a(N - N_0)$, where a is the gain cross-section and N_0 is the transparency value for the carrier density ($g = 0$ at $N = N_0$). Other parameters include the group velocity of the light travelling in the semiconductor v_g, the mode propagation constant $k = n_{eff}k_0$ where n_{eff} is the effective (modal) index of refraction and $k_0 = \omega/c$ is the free-space propagation constant, the internal loss α_{int}, the linewidth-enhancement factor α, the transverse confinement factor Γ, the Kerr nonlinearity $n_2 = \Gamma n_2^{act} + (1 - \Gamma)n_2^{clad}$ where n_2^{act} and n_2^{clad} are the material Kerr coefficients of the active and cladding layers respectively, the diffusion constant D, the injected current density J, the magnitude of the electron charge q, the active-layer thickness d, the nonradiative lifetime τ_{nr}, and is the spontaneous-emission coefficient B. Our choice of axes has the x-axis (lateral) parallel to the plane of the epitaxial layers, and perpendicular to the direction of the stripe contact, which is parallel to the z-axis (axial).

Because the carrier population affects the index of refraction as well as the optical gain, the linewidth-enhancement factor α couples changes in the gain to changes in the index of refraction. The α-parameter is one of the distinguishing aspects of semiconductor lasers since for all other types of lasers, modification of the gain results in negligible changes in refractive index.

Equations (1)-(3) not only account for the spatial variance of and coupling between counterpropagating waves and carriers, but also include diffraction, carrier-induced index variations, free-carrier absorption, material gain, self-focusing ($n_2 > 0$) or self-defocusing ($n_2 < 0$) through a Kerr-type nonlinearity, carrier injection, diffusion, gain saturation, and nonradiative, spontaneous, and stimulated recombinations. The rest of our theoretical and computer modelling will be based on this set of equations.

Using Equations (1)-(3), we first create an analytic model[17] for the filament gain in which several approximations are made. First, we consider an infinitely wide current stripe. This has the implications of not being able to predict effects due to the edges of the current injection stripe, the ramifications of which we have already seen in comparison to the measurements. Second, to avoid solving a complicated boundary-value problem, we assume that mirror losses are distributed throughout the cavity. We consider field propagation only in the forward direction by unfolding the Fabry-Perot cavity. The intracavity field then satisfies a modified version of Eqn. (1) where there is only one field, and α_{int} is replaced by $\alpha_{cav} = \alpha_{int} + \ln(R_0R_L)/2L$. The equation for the carrier distribution is modified to create an effective carrier lifetime $\tau = (1/\tau_{nr} + BN_{th})^{-1}$.

Once the device reaches threshold in the steady-state regime, the carrier density becomes clamped at its threshold value, and thus the gain becomes clamped at a value which exactly compensates for the cavity loss[18]. Using this condition and the fact that our assumption of an infinitely wide current stripe dictates that the carrier density be uniform in the x-direction, the threshold carrier density under cw operation is given by $N_{th} = N_0 + \alpha_{cav}/(\Gamma a)$. Using this expression and neglecting diffraction for an infinitely wide current stripe, we can rewrite the field equation in the steady state, using the mean-field approximation and replacing $|E|^2$ by an average value, to obtain the solution $E = \sqrt{I}\,\exp(i\beta z)$, where I is the intracavity mean-field intensity, and β is the modification to the propagation constant.

Using the steady-state forms for the field and carrier density, Eqn. (3) gives an expression that relates the intracavity intensity to the injected current density. Since the intensity is negligible near threshold, we can readily determine the threshold current density $J_{th} = qdN_{th}/\tau$. Combining this with Eqn. (3) and defining a pump parameter $r = J/J_{th}$, we arrive at a solution for the intracavity intensity in terms of the pumping level r as $I = I_s(r-1)/(1-N_0/N_{th})$ where $I_s = \hbar\omega/(\Gamma a\tau)$ is the saturation intensity.

Now, we examine the stability of these cw solutions to small perturbations. The steady-state solution is stable if small perturbations decay with time, while their growth signifies that the cw solution is unstable. We follow the standard procedure for linear stability analysis and linearize the modified Eqns. (1) and (3) in terms of small, perturbative parameters ε and n defined as $E = [\sqrt{I} + \varepsilon(x, z, t)]\exp(i\beta z)$ and $N = N_{th} + n(x, z, t)$. Linearizing these equations in in ε and n, and using the steady-state solutions, yields a set of two coupled linear equations which can be easily solved by using the Fourier method. Each Fourier component of ε corresponds to a plane-wave perturbation of the form $\exp[i(k_x x + k_z z - \Omega t)]$ where k_x is the spatial frequency of the perturbation, Ω is its oscillation frequency, and k_z is the propagation constant to be determined by solving the linearized equations. Further, we note that since ε represents a complex field, it is determined be two independent variables, which can be amplitude and phase, real and imaginary parts[3], or complex conjugates[19]. By examination of the linearized equations, the latter seems to be the best choice. By eliminating the carrier density perturbation, we arrive at two coupled algebraic equations for ε and ε^*. An equation for k_z yields the only non-trivial solution, from which the filament gain can be extracted from the imaginary part k_z by using $g = -2\mathrm{Im}(k_z)$. The factor of 2 is used to define power gain to obtain

$$g = \mathrm{Re}\left\{ \sqrt{\frac{2k_x^2}{k}\left[\alpha_{eff}G + 2n_2k_0 I - \frac{k_x^2}{2k}\right] + G^2} \right\} - G. \tag{4}$$

where the effective value of the linewidth-enhancement factor has been defined as

$$\alpha_{eff} = \frac{\alpha - \Omega\tau/(1 + I/I_s + D\tau k_x^2)}{1 + \alpha\Omega\tau/(1 + I/I_s + D\tau k_x^2)}\ , \tag{5}$$

and the saturated power gain is given by

$$G = \Gamma g(N_{th})\frac{(I/I_s)(1 + I/I_s + D\tau k_x^2 + \alpha\Omega\tau)}{(1 + I/I_s + D\tau k_x^2)^2 + (\Omega\tau)^2}\ . \tag{6}$$

For filamentation to occur, the gain must exceed the cavity loss, making the perturbative Fourier components grow exponentially with propagation, thereby destabilizing the cw solution. This is the origin of filamentation in semiconductor lasers. The spatial frequency k_x of filamentation is related to the filament spacing $2\pi/k_x$, while a non-zero value of the frequency Ω implies that the filaments are oscillating in time with a frequency $\Omega_{fil} = |\Omega|/2\pi$.

Equation (4) describes the gain of the instability as a function of the filament spacing and oscillation frequency, as well as the linewidth-enhancement factor, nonlinear refractive index, and pumping level through the intracavity intensity I. By comparing the terms within the radical sign, we can draw several general conclusions. It is readily seen that the filament gain increases with the linewidth-enhancement factor α, yet a highly saturated gain will reduce its effect. This feature can be understood by noting that as the gain where the filament is located saturates, the regions surrounding the filament will experience more gain, thereby allowing the surrounding regions to increase in intensity. A similarly combative effect is that of diffraction, as can be noted from the terms under the radical. Moreover, the more closely spaced the filaments are, the larger effect diffraction will have. Thus, we can expect diffraction to play a significant role in determining the filament spacing. Carrier diffusion plays a role similar to both diffraction and gain saturation in that the carriers, which are responsible for the α-induced self-focusing, tend to disperse in such a way as to reduce spatial modulations, thus reducing spatial index modulations directly. The nonlinear index n_2 can have detrimental or beneficial effects, depending on its sign. It has been shown that positive values of n_2 will lead to filamentation through self-focusing, thus enhancing the effect of the linewidth-enhancement factor[20]. However, note that a negative value of this parameter will help to combat filamentation through self-defocusing, thus counteracting the carrier-induced self-focusing governed by the linewidth-enhancement factor.

The instability gain given by Eqn. (4) is a complicated function of many variables. Although the surface in the spatio-temporal domain is complicated, the key feature is that there is an absolute maximum. This maximum will shift in the space-time domain for various parameter variations, namely the linewidth-enhancement factor α and the pump parameter r. For filamentation to occur, the filament gain must exceed the cavity loss. What determines the filament spacing and frequency in a given laser? The answer to this question is that the perturbation for which the gain is maximum would grow fastest and would dominate the growth process. This is the method that was used to calculate the curves shown with the data in Figs. (1)-(3).

However, we have already seen in Fig. (3) that the stripe width, not included in our analytic model, plays an important role in determining the properties of filamentation. We thus implement numerical simulations using Eqns. (1)-(3), (neglecting the time-depencence in order to save computation time) while investigating the onset of filamentation. These equations are solved iteratively using a split-step Fourier (or beam propagation) method[2, 22, 23]. We use the boundary conditions $E_f(x,0) = \sqrt{R_0}\ E_b(x,0)$ and $E_b(x,L) = \sqrt{R_L}\ E_f(x,L)$ to relate the forward and backward propagating beams at the facets, where R_0 and R_L represent the facet power reflectivities at $z = 0$ and $z = L$ respectively. The iteration procedure is initiated by using a super-Gaussian lateral profile at $z = 0$. The carrier density is calculated laterally for each step in the propagation using a tridiagonal matrix method. The lateral mode profile changes initially during multiple round trips inside the laser cavity and settles down to a fixed shape after 15-25 round trips if a stable lateral mode exists for a given set of operating parameters. Our convergence criteria rest on comparing the changes in the output power and the lateral mode width on successive round trips. If the lateral mode does not stabilize even after 100 round trips and exhibits filamentary structure, the laser is quantified as "unstable" for that set of operating parameters.

For numerical purposes, it is useful to show results as a function of J/J_{th}, where J is constant over the stripe width w and zero outside the stripe, and J_{th} is the threshold current density. Since the field is negligible below threshold, the last term in Eqn. (3) can be neglected. However, J_{th} depends on the stripe width w because of carrier diffusion. For simplicity, we solve for the threshold current density from Eqn. (3) by neglecting carrier diffusion and the time derivative. The result is $J_{th} = (qdN_{th}/\tau_{nr})\ [1 + B\tau_{nr}N_{th}]$, where $N_{th} = N_0 + (\alpha_{mir} + \alpha_{int})/(a\Gamma)$ with $\alpha_{mir} = -\ln(R_0R_L)/L$ can be obtained by equating the gain and losses of the system[18]. This simple model of threshold does not apply for narrow stripes ($\lesssim 10\ \mu m$) which can yield device thresholds higher than the calculated value (because of carrier diffusion), but it allows us to define a pump parameter $r = J/J_{th}$ which is constant with respect to the stripe width. This is equivalent to scaling the total injected current directly with the stripe width. The parameter values used for calculations and simulations in the upcoming sections are appropriate for an AlGaAs semiconductor laser operating near 820 nm.

4. FILAMENTATION CONTROL: α REDUCTION

Now that we have several theoretical tools with which to study filamentation, it is prudent to first examine the parameter space for the linewidth-enhancement factor since it is well known α plays an important role in destabilizing the lateral mode and producing filamentation[6, 7]. Using our analytic formalism of the filament gain, we can study how the gain maximum varies with the linewidth-enhancement factor and the pumping level. Figure 4 displays plots of the peak gain as a function of r for various α. In this figure, the dashed horizontal line represents the loss level which the filament gain must exceed in order for filamentation to dominate the behavior of the laser. Several points are clear from this figure. First, for pumping levels just above threshold, no filamentation will take place, as has been noted in practice. Second, and most importantly, there is a non-zero value for the linewidth-enhancement factor below which the laser is stable even when pumped ten times above. From Eqn. (4), we can infer that this stability region exists with $\alpha > 0$ due to the spreading effects of diffraction, gain saturation, and carrier diffusion. The physics represented in Fig. 4 indicate that increasing either pumping or the linewidth-enhancement factor will increase the tendency for filamentation, as has also been noted in practice. Note that combining this result with the data in Fig. 1 indicates that the decreased filament spacing is directly linked to increased filament gain.

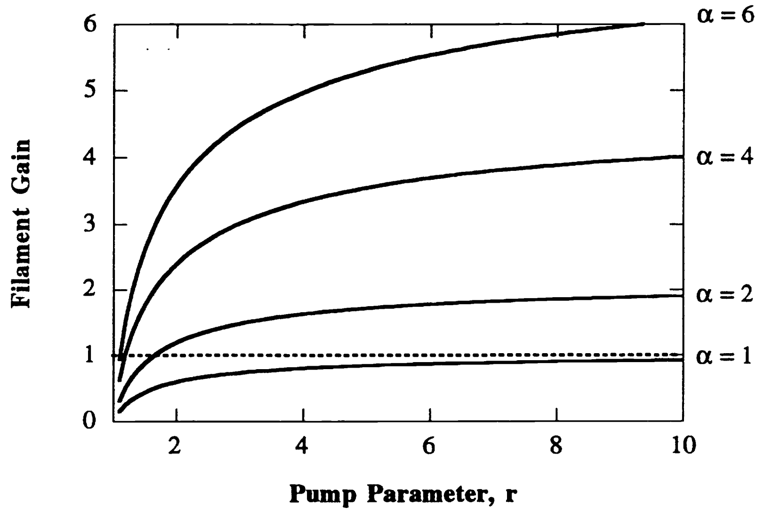

FIGURE 4. Filament gain maxima (normalized to the cavity loss α_{cav}) vs. r for various α with $n_2 = 0$. The dashed line represents the cavity loss which the gain must exceed for the laser to exhibit filamentation.

With the insight provided from our analytic model, it is now useful to turn to simulations and include the effect of the width of the current stripe w for a more accurate prediction of the value of α below which filamentation can be avoided. Figure 5 shows the regions of stable and unstable operations in the w-α plane for three different applied current densities. Several conclusions can be drawn from Fig. 5. First, semiconductor lasers with any value of α are stable for narrow stripes ($\lesssim$ 6 μm). Second, the critical width at which the device will operate stably depends on the level of pumping; increased levels of pumping reduce the critical width at which a laser can operate stably. Third, for a given pump level, variations in α around typical device values (α ~ 2-5) do not change this critical stripe width much, and this feature has been noted in practice for device fabrication. Fourth, for wide stripes, the critical linewidth-enhancement factor below which the laser operates stably remains fairly constant, and is not affected much by

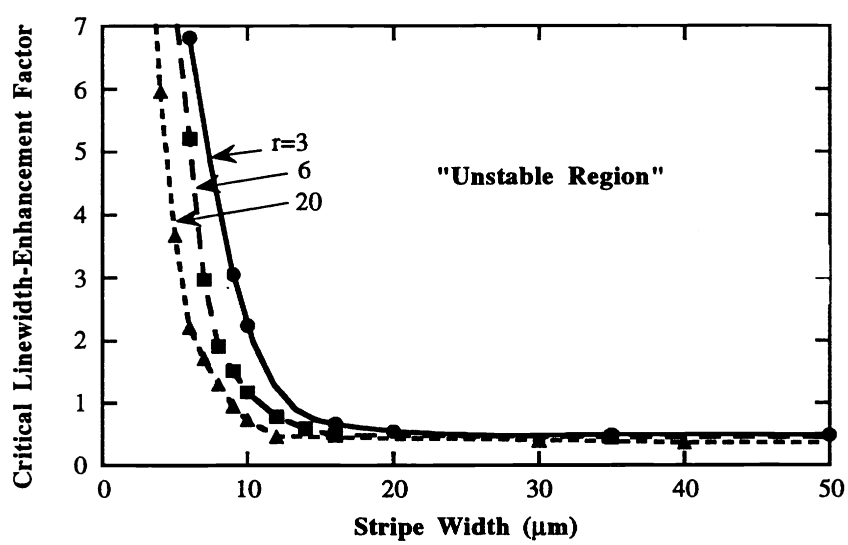

FIGURE 5. Stable operation boundaries in the w-α plane. The curves are critical values of α for which the lateral mode becomes unstable at a given stripe width w for r = 3 (solid curve), r = 6 (dashed curve), and r = 20 (dotted curve).

different injected current densities, as predicted by the analytic model. We have verified numerically that this behavior persists for stripes as wide as 250 μm. The key feature of Fig. 5 is that for values of the linewidth-enhancement factor below ~0.5, the laser will remain stable for very wide stripe widths at a pumping level as high as 20 times threshold. This stability region is due to the mechanisms which fight against filamentation, namely diffraction, gain saturation, and diffusion.

5. FILAMENTATION CONTROL: α NEGATION

So far, we have predicted regions in the α-r parameter space where the laser will be free of filamentation. As alluded to earlier, the effect of the nonlinear index of refraction can be beneficial or detrimental, depending on its sign. Gain saturation induces a local increase in the refractive index due to the linewidth-enhancement factor, as can be seen from Eqns. (1) and (2). Through the Kerr nonlinearity, this α-induced self-focusing can then be either enhanced by self-focusing ($n_2 > 0$) or reduced by self-defocusing ($n_2 < 0$). Using the analytic model of the filament gain, Figure 6 displays filament spacing for a laser with $\alpha = 2$ and a varying value of n_2 for several pumping levels. It is readily seen that the effects of a positive nonlinear index are similar to those caused by increasing α: the filaments become more tightly spaced. The interesting behavior appears when $n_2 < 0$. For small values, self-defocusing has the same effect as reducing α by increasing the filament spacing. However, as the self-defocusing become stronger, we notice that there is a transition to a large spacing, as seen in Fig. 6. The model predicts filament spacings > 1 mm, values which are larger than typical stripe widths (~100 μm) of broad-area lasers. What the rapid rise in filament spacing indicates is that there can only be one filament under the current stripe, hence unfilamented, single-lateral-mode behavior.

However, due to our assumption of an infinitely wide stripe, these results must be used with caution. In order to verify these results while including the effect of the stripe width, we turn to the numerical model[21]. For a given stripe width w and a given pumping level $r = J/J_{th}$, we vary n_2 over the range -1-10 x 10^{-12} cm²/W and find the critical boundary values of α beyond which the lateral mode destabilizes. The results are plotted in the n_2-α plane after slight averaging to remove the numerical noise associated with finite step sizes. Figure 7 shows the stability region at two different pumping levels (r = 2.5 and 5) for a stripe width of 50 μm. For r = 2.5, the main effect of the self-focusing nonlinearity is to increase the critical value of α from 0.5 to above 2 for $(1 - \Gamma)|n_2| > 8 \times 10^{-12}$ cm²/W. At higher pumping levels (r = 5), the critical value of α can exceed 2 for $(1 - \Gamma)|n_2| > 5 \times 10^{-12}$ cm²/W. However, a new qualitative feature appears showing that for large values of $|n_2|$, the lateral mode can become unstable even for small values of α. This can be understood by noting that α-induced and n_2-induced changes in the mode index are of opposite sign, and the two must be balanced for realizing stable operation of broad-area semiconductor lasers.

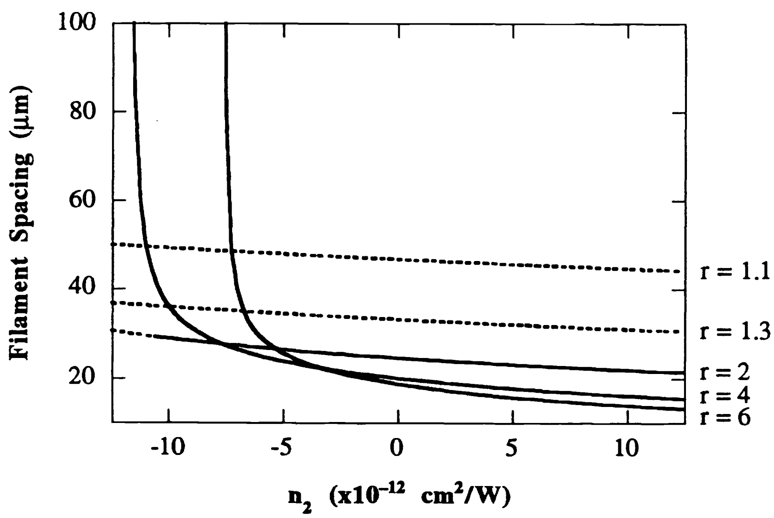

FIGURE 6. Filament spacing as a function of n_2 for various pumping levels r with $\alpha = 2$. The dashed portions of the curves indicate that the gain is less than the cavity loss and that filamentation will not occur.

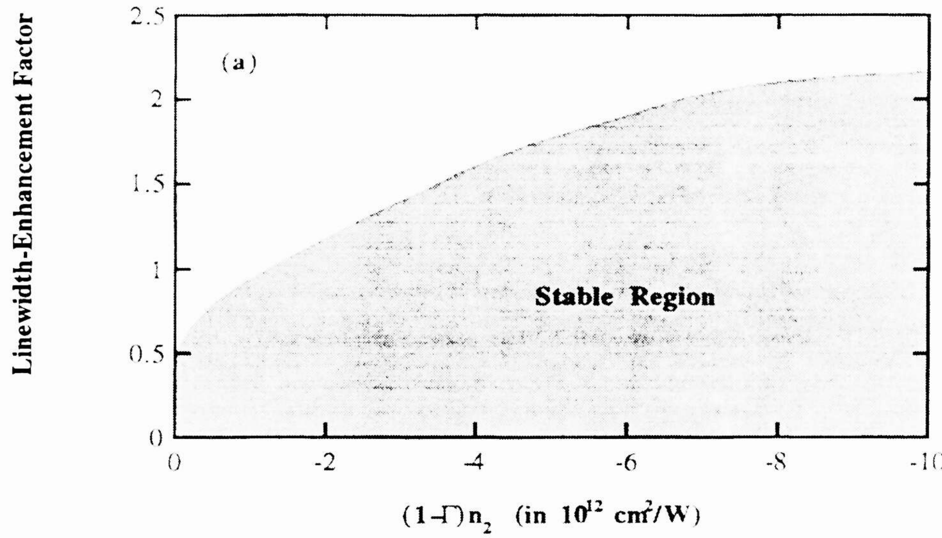

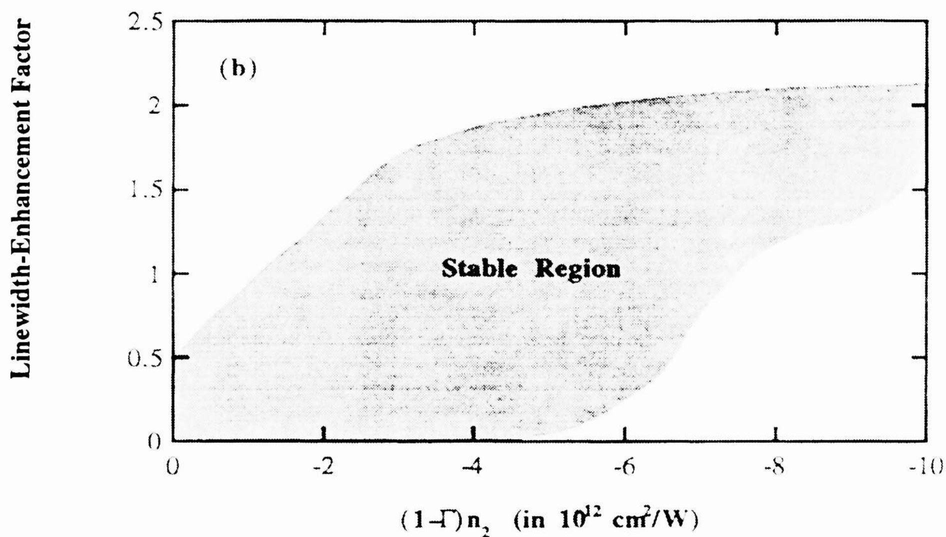

FIGURE 7. Stable operation regions in the n_2-α plane for a 50-μm stripe-width laser operating (a) 2.5 times above threshold and (b) 5 times above threshold. The boundaries of these regions mark the values of α for which the lateral mode becomes unstable at a given value of n_2.

To underscore the mode quality, Figs. 8(a) and 8(b) show the near-field and far-field profiles respectively for laser operation at 2.5 times above threshold when $\alpha = 1$, and $(1 - \Gamma)n_2 = -5 \times 10^{-12}$ cm²/W. For $n_2 = 0$, the numerically simulated mode exhibits filamentary structure. We can see from Fig. 8(a) that n_2 has indeed suppressed the catastrophic self-focusing that leads to filamentation. However, this α-induced self-focusing is not completely quenched as noted by the "squeezing" near the center of the current stripe. The twin-lobed far-field profile shown in Fig. 8(b) is evidence of a curved wavefront, which is a typical feature of such gain-guided devices[18]. As the injected current is increased to 5 times above threshold, the device remains in the stable region shown in Fig. 7(b). However, the effective index reduction in the self-defocusing layers has increased since it depends on n_2 times the mode intensity. Figures 8(c) and 8(d) display the near- and far-field profiles respectively for this case. Notice that n_2 has completely compensated for any α-induced self-focusing as evident by the flatness of the lateral mode profile over the width of the current stripe. Another key point is that the far-field is single-lobed. Thus, n_2 has also removed the astigmatic curvature that is typically found in gain-guided semiconductor lasers. From a practical standpoint, Fig. 8 shows that as long as the device remains within the stable region of operation, the lateral mode profile can be tailored by adjusting the injection current.

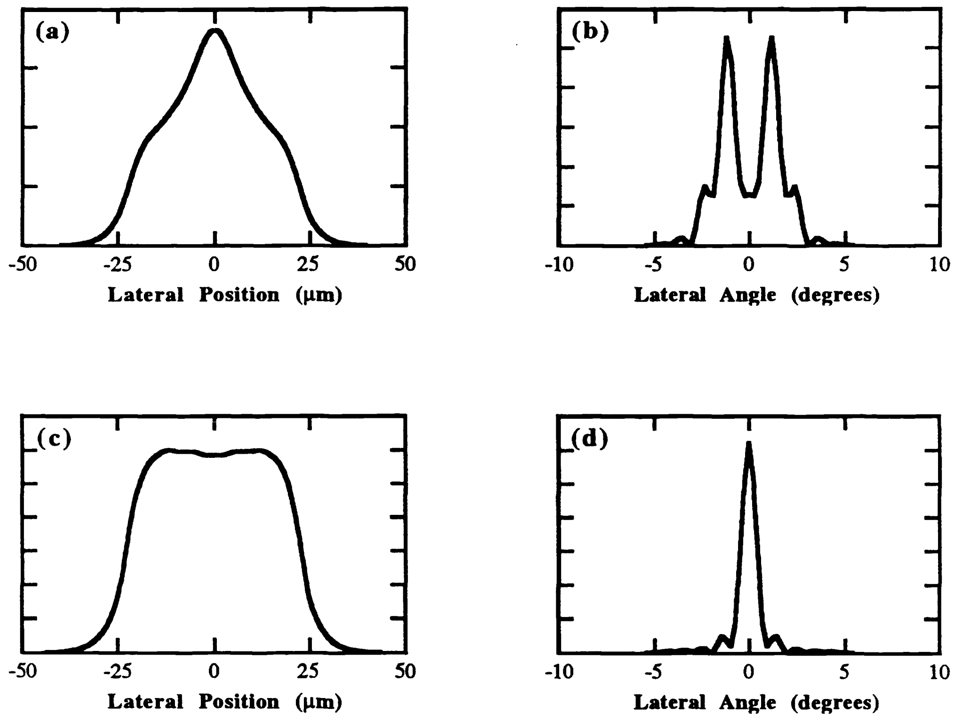

FIGURE 8. Normalized near-field (left column) and far-field (right column) profiles for a 50-μm stripe-width laser operating 2.5 times above threshold (upper row) and 5 times above threshold (lower row). In both cases $\alpha = 1$ and $n_2 = -5 \times 10^{-12}$ cm^2/W.

For high output powers, it is desirable to widen the stripe as much as possible. Figure 9 shows the stability regions for a 100-μm stripe at $r = 2.5$ and 5. The qualitative behavior is similar to the 50-μm stripe case except that the stability region is reduced at a given pumping level. This behavior can be understood by noting that the n_2-induced index change becomes so large at high pumping levels that it introduces its own set of instabilities which become severe for relatively wide stripes[20]. Correspondingly, we expect this stability region to shrink as the stripe width is increased. From a design perspective, the optimum value of n_2 depends on both the stripe width w and the pumping level for a given value of α.

A source for the negative intensity-dependent refractive index ($n_2 < 0$) can come from below-bandgap nonlinearities found by designing a new pair of epitaxial layers, sandwiched between the active and cladding regions, for which the bandgap is close to but less than the lasing wavelength. Even though these new layers would be transparent to the intracavity radiation due to their larger bandgap energy, a large fraction (80-99%) of the lateral mode would reside in them and experience a nonlinear index change resulting from the third-order susceptibility. Experimentally measured values of n_2 for AlGaAs near the 0.8 μm wavelength region are in the range $n_2 = -4\text{-}8 \times 10^{-12}$ cm^2/W depending on the Al content[24, 25], with similar values reported for InGaAsP near 1.5 μm[26, 27].

How can one implement these numerical results for designing a laterally-stable device? In recent years, there have been several reports of devices with values of $\alpha < 2$. Using a multiple-quantum-well (MQW) structure with strained active regions, one group was able to produce a laser with a measured value $\alpha = 1$[28]. We propose to use a pair of self-defocusing layers of thickness ~0.1 μm sandwiched between the MQW active region and the cladding layers. For example, to achieve a value of $n_2 = -5 \times 10^{-12}$ cm^2/W, the bandgap of the new layers should be larger than that of the active layers by 29 meV[24]. This bandgap difference is large enough that it should not affect carrier injection into the quantum wells significantly. In fact, a simple calculation for the density of states of such a quantum well[18] shows that the carrier density in the active layers is large enough to sustain lasing. However, note that thermal activation may induce carrier leakage, thereby increasing the device threshold.

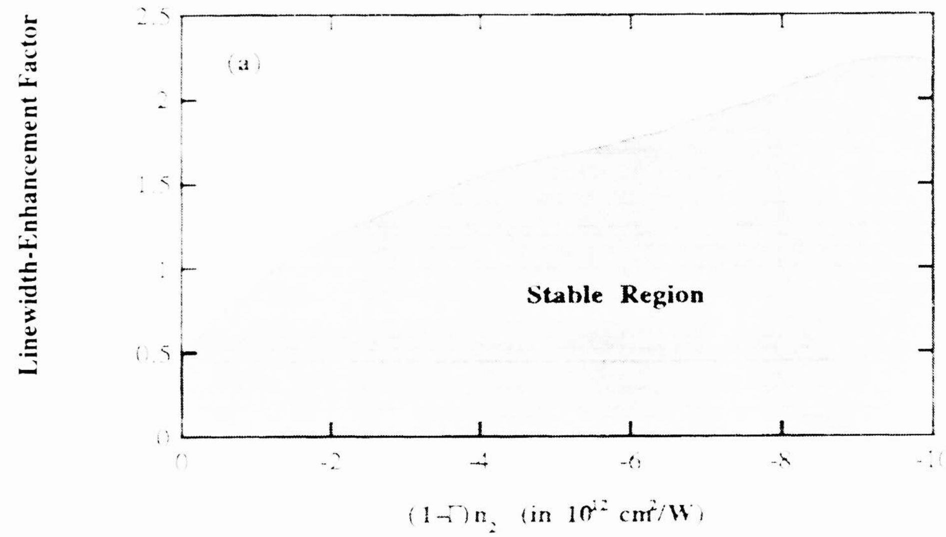

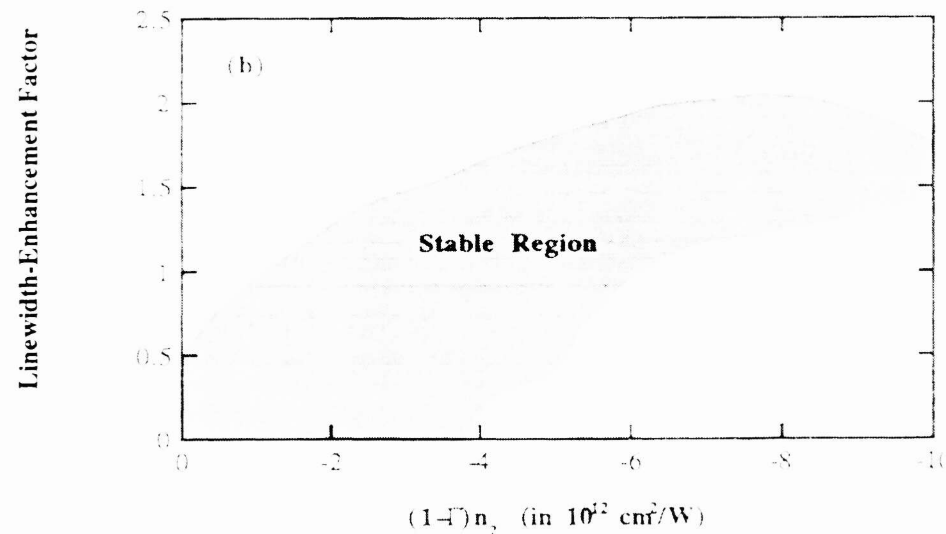

FIGURE 9. Same as in Fig. 7 except the stripe width has been changed to 100 μm for (a) 2.5 times above threshold and (b) 5 times above threshold.

6. CONCLUSIONS

We experimentally measured the first-order spatio-temporal characteristics of filamentation and discovered effects of the stripe width. We used an analytic theory to explain and reproduce these results through an expression for the filament gain, in which contributions of various mechanisms can clearly be seen. Both experiment and model showed that as the pumping level or linewidth-enhancement factor is increased, the filament gain is increased leading to a decrease in the filament spacing.

Through this analytic theory and computer simulations, we determined the stability boundaries of for various stripe widths and operating levels for which the device will not exhibit filamentary tendencies. It was also shown that there is a value for the linewidth-enhancement factor below which the devices are stable for wide stripe widths and high pumping levels. Unfortunately, the required value of $\alpha < 0.5$ is too low to be realistic for current state-of-the-art semiconductor lasers. However, we should note that the effective value of α is generally different than the material value of α[11], and it may be possible to design a broad area laser such that the effective α is below the critical value. Such devices will be stable without filamentation, regardless of stripe width or injection current.

We then proposed a new method of controlling filamentation using below-bandgap semiconductor nonlinearities occurring inside new epitaxial layers. With simulations, we determine under what conditions this imposed nonlinearity can counteract the carrier-induced self-focusing inside the active region. This nonlinearity can be used to stabilize the lateral mode by tailoring the bandgap difference between the active and the new self-defocusing layers. We have suggested the design of such a laterally-stable broad-area laser by using a strained MQW active region since α values are relatively low for such structures. Although our simulations considered broad-area semiconductor lasers, qualitatively similar behavior is expected to occur for amplifier and MOPA devices.

7. REFERENCES

1. R. W. Boyd, *Nonlinear Optics*. Boston: Academic Press, 1992.
2. G. C. Dente and M. L. Tilton, *IEEE J. Quantum Electron.*, **20**, 76-88 (1993).
3. A. H. Paxton and G. C. Dente, *J. Appl. Phys.*, **70**, 1-6 (1991).
4. L. Goldberg, M. R. Surette, and D. Mehuys, *Appl. Phys. Lett.*, **62**, 2304-2306 (1993).
5. R. J. Lang, D. Mehuys, D. F. Welch, and L. Goldberg, *IEEE J. Quantum Electron.*, **30**, 685-693 (1994).
6. R. J. Lang, D. Mehuys, A. Hardy, K. M. Dzurko, and D. F. Welch, *Appl. Phys. Lett.*, **62**, 1209-1211 (1993).
7. H. Adachihara, O. Hess, E. Abraham, P. Ru, and J. V. Moloney, *J. Opt. Soc. Am. B*, **10**, 658-665 (1993).
8. O. Hess, S. W. Koch, and J. V. Moloney, *IEEE J. Quantum Electron.*, **31**, 35-43 (1995).
9. J. R. Marciante and G. P. Agrawal, *IEEE Photon. Technol. Lett.*, vol. 10, January, 1998.
10. I. D. Henning, and J. V. Collins, *Electron. Lett.*, vol. 19, pp. 927-929 (1983).
11. S. S. Lee, L. Figueroa, and R. Ramaswamy, *IEEE J. Quantum Electron.*, vol. 25, pp. 862-870 (1989).
12. M. P. van Exter, W. A. Hamel, J. P. Woerdman, and B. P. Zeijlmans, *IEEE J. Quantum Electron.*, vol. 28, pp. 1470-1478 (1992).
13. A. Schönfelder, S. Weisser, J. D. Ralston, and J. Rosenzweig, *IEEE Photon. Technol. Lett.*, vol. 6, pp. 891-893 (1994).
14. W. Rideout, B. Yu, J. LaCourse, P. K. York, K. J. Beernick, and J. J. Coleman, *Appl. Phys. Lett.*, vol. 56, pp. 706-708 (1990).
15. R. Raghuraman, N. Yu, R. Engelmann, H. Lee, and C. L. Shieh, *IEEE J. Quantum Electron.*, vol. 29, pp. 69-75 (1993).
16. D. J. Bossert and D. Gallant, *IEEE Photon. Technol. Lett.*, vol. 8, pp. 322-324 (1996).
17. J. R. Marciante and G. P. Agrawal, *IEEE J. Quantum Electron.*, vol. 33, pp. 1174-1179, (1997).
18. G. P. Agrawal and N, K, Dutta, *Semiconductor Lasers*, 2nd ed. New York: Van Nostrand Reinhold, 1993.
19. C.-J. Chen, P. K. A. Wai, and C. R. Menyuk, *Opt. Lett.*, **20**, 350-352 (1995).
20. J. R. Marciante and G. P. Agrawal, *IEEE J. Quantum Electron.*, **32**, 90-596 (1996).
21. J. R. Marciante and G. P. Agrawal, *Appl. Phys. Lett.*, **69**, 593-595 (1996).
22. G. P. Agrawal, *J. Appl. Phys.*, **56**, 3100-3109 (1984).
23. M. Lax, J. H. Batteh, and G. P. Agrawal, *J. Appl. Phys.*, **52**, pp. 109-125 (1981).
24. M. J. LaGasse, K. K. Anderson, C. A. Wang, H. A. Haus, and J. G. Fujimoto, *Appl. Phys. Lett.*, **56**, 417-419 (1990).
25. G. I. Stegeman, "Nonlinear guided wave optics," chap. 1 in *Contemporary Nonlinear Optics*, ed. by G. P. Agrawal and R. W. Boyd. New York: Academic Press, 1992.
26. K. L. Hall, A. M. Darwish, E. P. Ippen, U. Koren, and G. Raybon, *Appl. Phys. Lett.*, **62**, 1320-1322 (1993).
27. A. D'Ottavi, E. Iannone, A. Mecozzi, S. Scotti, P. Spano, R. Dall'Ara, G. Guekos, and J. Eckner, *Appl. Phys. Lett.*, **65**, 2633-2635 (1994).
28. F. Kano, T. Yamanaka, N. Yamamoto, H. Mawatari, Y. Tohmori, and Y. Yoshikuni, *IEEE J. Quantum Electron.*, **30**, 533-537 (1994).